

Direct probing the quantum geometric tensor for bosonic collective excitations

Chi Wu,^{1,2} Takashi Oka,³ Shuichi Murakami,^{4,5,6} and Tiantian Zhang^{1,*}

¹*Institute of Theoretical Physics, Chinese Academy of Sciences, Beijing 100190, China*

²*University of Chinese Academy of Sciences, Beijing 100049, China*

³*The Institute of Solid State Physics, The University of Tokyo, Kashiwa, Chiba 277-8581, Japan*

⁴*Department of Applied Physics, University of Tokyo, 7-3-1 Hongo, Bunkyo-ku, Tokyo 113-8656, Japan*

⁵*International Institute for Sustainability with Knotted Chiral Meta Matter (WPI-SKCM²), Hiroshima University, Hiroshima, 739-8526, Japan*

⁶*Center for Emerged Matter Science, RIKEN, 2-1 Hirosawa, Wako, Saitama, 351-0198, Japan*

The quantum geometric tensor (QGT), whose real and imaginary parts define the quantum metric and Berry curvature, encodes the intrinsic geometry of quantum states. While electronic QGT has been directly observed and linked to various phenomena like electron-phonon coupling, its bosonic analogue remains both theoretically and experimentally unexplored. We demonstrate that the dynamical structure factor directly encodes the full QGT throughout the Brillouin zone, establishing it as a sensitive probe of both quantum metric and Berry curvature. Applying this framework, we uncover clear geometric signatures in a twofold quadrupole Weyl phonon in BaPtGe and the node-line magnon in Gd. Our results establish a general, direct route to measuring quantum geometry in bosonic systems, a crucial step toward elucidating its impact on condensed matter phenomena.

I. INTRODUCTION

Quantum geometry tensor (QGT) characterizes the intrinsic Hilbert-space structure of quantum states; its real and imaginary parts define the quantum metric tensor (QMT) and Berry curvature, respectively [1–5]. Direct observation of the QGT and its components is essential for elucidating its impact on condensed matter phenomena. For example, the Berry curvature governs topological phases and transport responses[6–9], while the quantum metric in electronic systems has emerged as a key ingredient in phenomena ranging from nonlinear Hall effects [10–15] to flat-band superconductivity [16–26], anomalous Landau quantization [27–29], and excitonic shifts [30–33], among others [34–48]. While the QMT has been experimentally accessed in artificial platforms [49–52] and solids via techniques such as angle-resolved photoemission spectroscopy (ARPES), these measurements have so far been confined to electronic bands [53, 54]. Consequently, direct experimental access to the QMT, and thus the full QGT, for bosonic collective excitations remains elusive. Bridging this gap is a crucial step toward understanding the role of quantum geometry in bosonic systems.

To overcome this challenge, we develop a general framework that enables direct access to the full QGT, including both the Berry curvature and quantum metric, of collective excitations via the dynamical structure factor (DSF) [55]. By formulating the DSF and QGT within a unified pseudospin framework, we establish a direct correspondence between measurable scattering intensities and the complete QGT. Although illustrated using two-band (subspace) Hamiltonians, the approach applies generally to multiband systems. As a universal probe of density-fluctuation-driven quasiparticles, the DSF enables a practical protocol, implementable with inelastic x-ray or neutron scattering, to resolve all components of

the bosonic QGT across the Brillouin zone. We demonstrate the approach with the twofold quadrupole Weyl phonon in BaPtGe [56, 57] and the nodal-line magnon in Gd [58], revealing clear signatures of quantum geometry.

II. BOSONIC QGT

The QGT is defined in a U(1)-gauge-invariant form as

$$\Omega_n^{ab}(\mathbf{k}) = \langle \partial_a n_{\mathbf{k}} | (1 - \hat{P}_n(\mathbf{k})) | \partial_b n_{\mathbf{k}} \rangle, \quad (1)$$

where $\hat{P}_n(\mathbf{k}) = |n_{\mathbf{k}}\rangle\langle n_{\mathbf{k}}|$ and $|n_{\mathbf{k}}\rangle$ is the periodic part of Bloch wavefunction in solids. Its real part is the quantum metric tensor (QMT, g_n^{ab}), which defines the distance between quantum states in Hilbert space; while its imaginary part gives the Berry curvature (Ω_n^{ab}).

For a minimal two-band model, $H(\mathbf{k}) = h_0\sigma_0 + \mathbf{h}(\mathbf{k}) \cdot \boldsymbol{\sigma}$, both Ω_n^{ab} and g_n^{ab} for each band takes a compact form in terms of the normalized pseudospin vector $\mathbf{d} = \mathbf{h}(\mathbf{k})/|\mathbf{h}(\mathbf{k})|$:

$$\begin{aligned} \Omega_{\pm}^{ab} &= \mp \frac{1}{2} \mathbf{d} \cdot \{ \partial_a \mathbf{d} \times \partial_b \mathbf{d} \} \text{ and} \\ g_{\pm}^{ab} &= \frac{1}{4} \partial_a \mathbf{d} \cdot \partial_b \mathbf{d}, \end{aligned} \quad (2)$$

where “ \pm ” donates the upper/lower band of the two-band system (Details are in the supplementary). Consequently, direct access to the pseudospin vector \mathbf{d} would immediately determine both Ω_n^{ab} and g_n^{ab} . In contrast to electronic systems, where circularly polarized ARPES can resolve the pseudospin [53, 54], the polarization of the incident probe usually does not directly imprint on the measured response of bosonic excitations. This essential difference rules out an ARPES-like strategy and calls for a fundamentally different approach.

We propose the dynamical structure factor as a direct probe of the bosonic QGT. While its explicit form depends on the specific system, the DSF admits a universal pseudospin representation. We illustrate this framework using phonons and magnons.

* ttzhang@itp.ac.cn

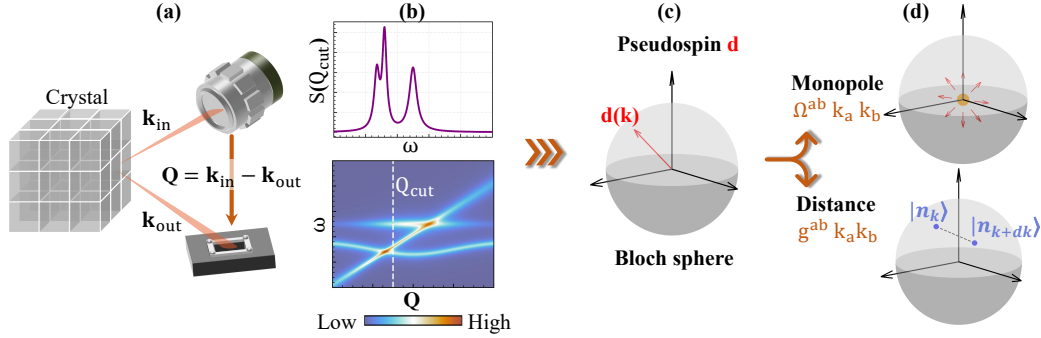


FIG. 1. Schematic illustration of the direct measurement of the Berry curvature and quantum metric tensor via the dynamical structure factor $S(\mathbf{Q}, \omega)$. (a) Experimental geometry for measuring $S(\mathbf{Q}, \omega)$. (b) Measured dynamical structure factor $S(\mathbf{Q}, \omega)$. (c) Pseudospin texture reconstructed from $S(\mathbf{Q}, \omega)$. (d) Berry curvature and quantum metric tensor derived from the pseudospin texture.

III. PHONON DSF AND QGT

The DSF characterizes a system's response to momentum- and energy-resolved probes, such as neutrons or x-rays [59–62]. As illustrated in Figs. 1(a)–(b), it encodes the spectrum of density fluctuations. The total DSF reads

$$S(\mathbf{Q}, \omega)_{\text{lp}} = N_{\text{cell}} \sum_{\mathbf{k}, \sigma} \frac{1}{\omega_{\mathbf{k}, \sigma}} \left| \sum_d \frac{f_d(\mathbf{Q})}{\sqrt{m_d}} e^{-W_d} \langle \mathbf{Q} \cdot \xi_d(\mathbf{k}) \rangle e^{i\mathbf{Q} \cdot \mathbf{r}_d} \right|^2 \times \left\{ (\langle n_{\mathbf{k}, \sigma} \rangle + 1) \delta(\omega - \omega_{\sigma}(\mathbf{k})) \delta(\mathbf{Q} - \mathbf{G} - \mathbf{k}) + \langle n_{\mathbf{k}, \sigma} \rangle \delta(\omega + \omega_{\sigma}(\mathbf{k})) \delta(\mathbf{Q} - \mathbf{G} + \mathbf{k}) \right\}. \quad (3)$$

Up to unimportant constant prefactors, the coherent contribution to the DSF for the s^{th} phonon mode reads

$$S_{\text{coh}}^{(s)}(\mathbf{Q}, \omega) \propto |F_{\text{coh}}^{(s)}(\mathbf{Q})|^2 = \left| \sum_d \frac{f_d(\mathbf{Q})}{\sqrt{m_d}} e^{-W_d} \mathbf{Q} \cdot \xi_d(\mathbf{k}) e^{i\mathbf{Q} \cdot \mathbf{r}_d} \right|^2. \quad (4)$$

$\mathbf{Q} = \mathbf{G} + \mathbf{k}$ denotes the total momentum transfer, $f_d(\mathbf{Q})$, m_d , W_d , \mathbf{r}_d and $\xi_d(\mathbf{k})$ represent the atomic form factor, mass of atom, Debye-Waller factor, equilibrium position, and s^{th} polarization vector of the d^{th} atom in the unit cell, respectively. For inelastic x-ray scattering, $f_d(\mathbf{Q})$ depends on momentum transfer \mathbf{Q} , whereas for neutron scattering it is a constant (the scattering length). Equation (4) reveals that the DSF is primarily governed by the factor $\mathbf{Q} \cdot \xi_d(\mathbf{k})$, which directly links the measured scattering spectra to the underlying microscopic dynamics, including the full phonon polarization structure.

To access the QGT through the DSF, one must first establish their connection via the pseudospin vector, as schematically shown in Fig. 1. For simplicity, we first consider a minimal two-band $k \cdot p$ model $H(\mathbf{k})$. Polarization vectors ξ transforming as irreducible representations are chosen as basis functions, yielding the model expressed as a direct sum of atomic contributions:

$$\begin{aligned} \xi^+ &= \oplus_d \xi_d^+, \\ \xi^- &= \oplus_d \xi_d^-. \end{aligned} \quad (5)$$

Thus, the polarization vector for the upper branch is

$$\xi^{\text{up}}(\mathbf{k}) = (\xi^+ \ \xi^-) \psi^{\text{up}}, \quad (6)$$

where $\psi^{\text{up}} = (\psi_+(\mathbf{k}) \ \psi_-(\mathbf{k}))^T$ denotes the normalized eigenvector.

Given that the DSF scales with the momentum transfer \mathbf{Q} , and experimental measurements often involve large \mathbf{Q} values lying beyond the first Brillouin zone, we decompose the wavevector as $\mathbf{Q} \approx \mathbf{G} + \mathbf{C}$. Here, \mathbf{G} is the reciprocal lattice vector, while \mathbf{C} denotes the coordinates of the relevant high-symmetry point within the first Brillouin zone. In the specific case of measurements near the Γ point, $\mathbf{C} = (0, 0, 0)$, leading to

$$\begin{aligned} |F_{\text{coh}}^{\text{up}}(\mathbf{Q})|^2 &= |\psi_+(\mathbf{k}) W^+(\mathbf{G}) + \psi_-(\mathbf{k}) W^-(\mathbf{G})|^2 \\ &= |\langle W | \psi^{\text{up}} \rangle|^2 \\ &= \frac{1}{2} |\mathbf{V}| \{1 + \cos(\mathbf{d}(\mathbf{k}), \mathbf{V}(\mathbf{G}))\} \\ &= \frac{1}{2} |\mathbf{V}| \{1 + \cos \theta_{\mathbf{k}} \cos \theta_{\mathbf{G}} + \sin \theta_{\mathbf{k}} \sin \theta_{\mathbf{G}} \cos(\phi_{\mathbf{k}} - \phi_{\mathbf{G}})\}, \end{aligned} \quad (7)$$

where $W^{\pm}(\mathbf{G}) = \sum_d \frac{f_d(\mathbf{Q})}{\sqrt{m_d}} e^{-W_d} \mathbf{G} \cdot \xi_d^{\pm} e^{i\mathbf{G} \cdot \mathbf{r}_d}$ are two components of $\langle W \rangle$. The vectors

$$\begin{aligned} \mathbf{d}(\mathbf{k}) &= \langle \psi^{\text{up}} | \sigma | \psi^{\text{up}} \rangle \\ &= (\cos \phi_{\mathbf{k}} \sin \theta_{\mathbf{k}} \ \sin \phi_{\mathbf{k}} \sin \theta_{\mathbf{k}} \ \cos \theta_{\mathbf{k}}) \text{ and} \\ \frac{\mathbf{V}(\mathbf{G})}{|\mathbf{V}(\mathbf{G})|} &= \frac{\langle W | \sigma | W \rangle}{|\langle W | W \rangle|} \\ &= (\cos \phi_{\mathbf{G}} \sin \theta_{\mathbf{G}} \ \sin \phi_{\mathbf{G}} \sin \theta_{\mathbf{G}} \ \cos \theta_{\mathbf{G}}) \end{aligned} \quad (8)$$

are the pseudospin for the states of ψ^{up} and $|W\rangle$, θ and ϕ are the spherical coordinates of the Bloch sphere. Thus, the coherent DSF in Eq. (7) provides a direct link to the pseudospin formulation of both the Berry curvature and the QMT in Eq. (2). We note that the pseudospin-based expression for the DSF in Eq. (7) is general and applies to arbitrary multiband systems, independent of topology or band gaps; details are in the supplementary.

In practice, the procedure begins by experimentally measuring the coherent DSF, $S_{\text{coh}}^{\text{up}}(\mathbf{Q}, \omega)$, as illustrated in Figs. 1(a)

and (b). From the measured DSF, the pseudospin vector $\mathbf{d}(\mathbf{k})$ is then reconstructed via polynomial fitting, as shown in Figs. 1(b) and (c). In practice, this reconstruction can be simplified by fitting the individual components $d_i(\mathbf{k})$ separately, which requires selecting Brillouin zones with well-polarized $\mathbf{V}(\mathbf{G})$. Alternatively, the pseudospin can be obtained by fitting the angular variables $\theta_{\mathbf{k}}$ and $\phi_{\mathbf{k}}$. The two approaches are formally equivalent, with their relative simplicity depending on the explicit form of $\mathbf{V}(\mathbf{G})$. Once the pseudospin texture is obtained, both the Berry curvature and the QMT follow directly. The DSF thus furnishes a concrete experimental observable for extracting the full phonon QGT.

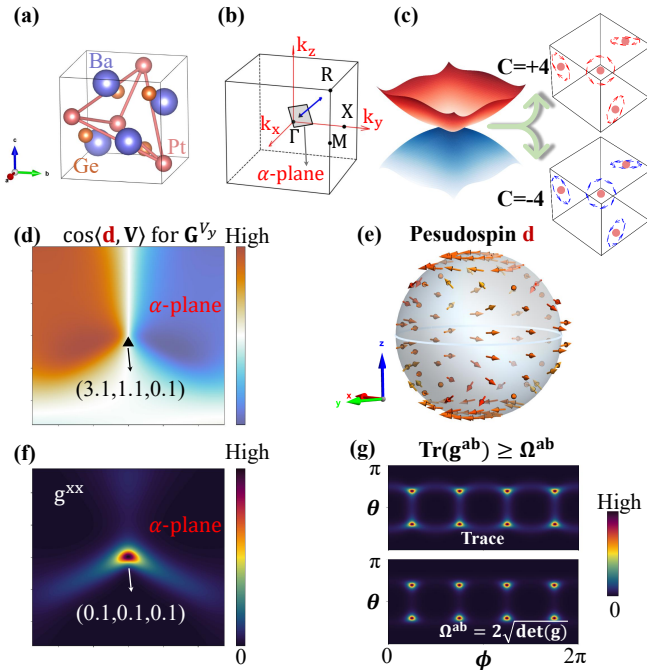


FIG. 2. (a) Crystal structure and (b) Brillouin zone for BaPtGe. The gray square cross section perpendicular to [111], denoted as the α plane, is centered at $(0.1, 0.1, 0.1)$ with side length 0.2. (c) The phonon dispersion of the TQW for BaPtGe, and the associated circularly polarized atomic motions for the two phonon branches. (d) The heat-map distribution of $\cos\langle\mathbf{d}, \mathbf{V}\rangle = \sin\theta_{\mathbf{k}} \sin\phi_{\mathbf{k}}$ obtained from the $k \cdot p$ model, plotted on the α plane in the Brillouin zone $\mathbf{G}^{V_y} = (3, 1, 0)$. (e) Pseudospin texture of \mathbf{d} on a sphere enclosing the TQW. (f) Distribution of the QMT component g^{xx} on the α -plane. (g) Distribution of the QMT trace and the Berry curvature on a sphere enclosing the TQW, both obtained from the pseudospin texture and represented in polar coordinates for the upper band.

IV. PHONON QGT IN BAPTGE

As an example, we next consider the twofold quadrupole Weyl (TQW) phonon at Γ in chiral cubic crystal BaPtGe [56, 57, 63], as shown in Figs. 2(a)-(c). We begin with a simplified $k \cdot p$ model and subsequently present the corresponding first-principles results. The effective model for the TQW is described by the Hamiltonian:

$$H_{\text{TQW}}(\mathbf{k}) = - \begin{pmatrix} Ak_x k_y k_z & B(k_x^2 + \omega^2 k_y^2 + \omega k_z^2) \\ B(k_x^2 + \omega k_y^2 + \omega^2 k_z^2) & -Ak_x k_y k_z \end{pmatrix}, \quad (9)$$

where $\omega = e^{-\frac{2\pi i}{3}}$, A and B are constants. As the TQW is mainly determined by the vibrations of Pt atoms at Wyckoff position $4a$ with $\mathbf{r}_0 = (c, c, c)$, we choose the basis states as (Details are in the supplementary):

$$\xi_d^{\pm} = \frac{1}{\sqrt{12}}((-1)^{\frac{(d+1)d}{2}}, (-1)^d \omega^{\pm 1}, (-1)^{\frac{(d-1)d}{2}} \omega^{\mp 1}), \quad (10)$$

associated atomic motions are shown in Fig. 2(c).

In the inelastic neutron scattering, $f_d(\mathbf{Q}) = b_{d,\text{coh}} = b_{\text{coh}}$. For a reciprocal lattice vector $\mathbf{G} = (g_x, g_y, g_z)$, we have

$$W^{\pm}(\mathbf{Q} \approx \mathbf{G}) = \frac{2\pi}{a} \frac{b_{\text{coh}} \cdot e^{-W}}{\sqrt{12m}} \cdot \{g_x A_1 + g_y \omega^{\pm 1} A_2 + g_z \omega^{\mp 1} A_3\}. \quad (11)$$

The polarization of $\mathbf{V}(\mathbf{G})$ depends on the summations A_1, A_2 and A_3 in Eq. (11), and is thus determined by both the atomic positions and the reciprocal lattice vector (Details are in the supplementary). Assume atoms are at the Wyckoff position $4a$ with coordinates of $\mathbf{r}_0 = (0.4, 0.4, 0.4)$, we identify the following reciprocal lattice vectors: $\mathbf{G}^{V_x} = (g_x + 2N, g_x, g_x)$, $\mathbf{G}^{V_y} = \{(4, 2, 0), (4, 0, 2), (3, 1, 0)\}$, and $\mathbf{G}^{V_z} = (2, 1, 4)$. $V_{x,y,z}$ means that $\mathbf{V}(\mathbf{G})$ is x -, y -, and z -polarized, respectively (Details are in the supplementary).

Figure 2(d) shows the heat-map distribution of $\cos\langle\mathbf{d}, \mathbf{V}\rangle = \sin\theta_{\mathbf{k}} \sin\phi_{\mathbf{k}}$ from the $k \cdot p$ model for $\mathbf{G}^{V_y} = (3, 1, 0)$, plotted on the α plane shown in Fig. 2(b). Using these distributions at different \mathbf{Q} , we extract the pseudospin components $d_{x,y,z}$, as shown in Fig. 2(e) (Details are in the Supplementary Material). Once $\mathbf{d}(\mathbf{k})$ is determined, the full quantum geometric tensor can be directly evaluated, such as the g^{xx} component shown in Fig. 2(f).

In this two-band model, the quantum metric g^{ab} encodes the same geometric volume as the Berry curvature Ω^{ab} , so that the Chern number and the determinant of the quantum metric coincide with the Berry curvature, i.e., $\Omega^{ab} = 2\sqrt{\det(g^{ab})}$, as shown in Fig. 2(g) in polar coordinates [20, 64–66].

V. SYMMETRY ANALYSIS AND DFT CALCULATIONS ON BAPTGE

The QGT for TQW in BaPtGe is constrained by the little co-group at the Γ point, which includes the twofold rotations $C_{2x,2y,2z}$, the threefold rotation $C_3^{[111]}$, and time-reversal symmetry \mathcal{T} . The corresponding transformation rules are summarized in the Supplementary Material. On the high-symmetry planes, these symmetries impose the following constraints:

$$\begin{aligned} g_{\pm}^{yz}(k_x, k_y, 0) &\xrightarrow{\mathcal{T}} g_{\pm}^{yz}(-k_x, -k_y, 0) \xrightarrow{C_{2z}} -g_{\pm}^{yz}(k_x, k_y, 0), \\ g_{\pm}^{xz}(k_x, k_y, 0) &\xrightarrow{\mathcal{T}} g_{\pm}^{xz}(-k_x, -k_y, 0) \xrightarrow{C_{2z}} -g_{\pm}^{xz}(k_x, k_y, 0). \end{aligned} \quad (12)$$

Thus, the components g_{\pm}^{ac} and g_{\pm}^{bc} must vanish on the corresponding $k_c = 0$ plane. At the intersections of these planes, i.e., along the twofold rotation $C_{2x,2y,2z}$ axis, all QMT components are constrained to be zero (Details are in the supplementary). Along the threefold rotational axis, where $\mathbf{k}' = C_3^{[111]}\mathbf{k} = \mathbf{k}$, all diagonal components of the QMT become equal and all off-diagonal components likewise equal, subject to the constraint $g_{\pm}^{xx} + 2g_{\pm}^{xy} = 0$. This reflects the z -polarized pseudospin structure along the [111] direction.

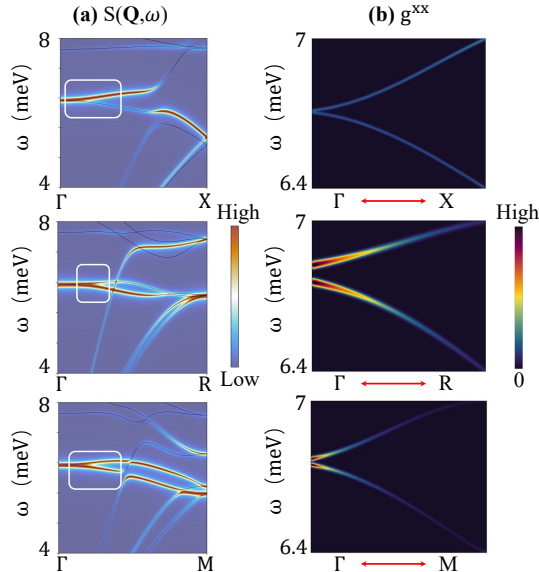


FIG. 3. (a) DSF with $\mathbf{G} = (0, 3, 3)$ and (b) QMT component g^{xx} for the TQW in BaPtGe along three high-symmetry lines, obtained from first-principles calculations. It is evident that the QMT is zero along the C_2 -invariant line $\Gamma - X$.

Figure 3 shows the DSF and the g^{xx} component of the QMT for BaPtGe from first-principles calculations. Consistent with the symmetry constraints discussed above, g_{\pm} vanishes along $\Gamma - X$ (top panel in Fig. 3 (b)), while it has only one independent component along $\Gamma - R$, i.e., $g_{\pm}^{xx} = g_{\pm}^{yy} = g_{\pm}^{zz} = -2g_{\pm}^{xy} = -2g_{\pm}^{yz} = -2g_{\pm}^{zx}$. Consequently, knowledge of g^{xx} alone suffices to reconstruct the full QMT (middle panel in Fig. 3 (b)). Along $\Gamma - M$ (on the $k_z = 0$ plane), fewer independent components exist, with $g_{\pm}^{xx} = -g_{\pm}^{xy}$; the full QMT can nonetheless be reconstructed by additionally computing g^{zz} and g^{xz} . Thus, the full QMT, and hence the complete QGT, in phonon systems can be directly extracted from DSF measurements.

VI. MAGNON DSF IN GADOLINIUM

Elemental gadolinium (Gd) has been reported to host both node-line magnons (along $H - K$) and node-plane magnons (on the $q_z = \pi$ plane) [58, 67], as shown in Figs. 4 (a)-(b). Near the magnon Dirac cone at the K point, inelastic neutron scattering (INS) exhibits an anisotropic intensity pattern, which is well captured by linear spin-wave theory (LSWT) and the two-band $k \cdot p$ model below:

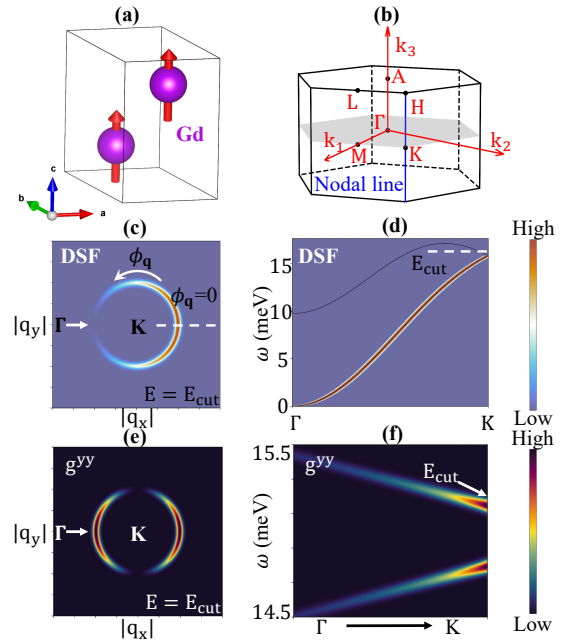


FIG. 4. (a) Crystal structure and magnetic order of Gd. (b) Brillouin zone and the location of node-line magnon. DSF for the node-line magnon with $\mathbf{G} = (0, 0, 2)$ on (c) a q -plane with the constant-energy surface (E_{cut}) in momentum space and (d) along the $\Gamma - K$. (e)-(f) g^{yy} obtained by the DSF in (c) and (d), respectively.

$$H_K(\mathbf{q}) = \epsilon_0(\mathbf{q})\sigma_0 + A \cos \frac{q_z}{2} (q_x\sigma_x + q_y\sigma_y), \quad (13)$$

where \mathbf{q} is the effective wavevector measured from the K point. The z -component pseudospin of this model is confined to be zero, corresponding to condition $\theta_{\mathbf{q}} = \pi/2$ in Eq. (7). Within the linear approximation, q_z controls only the tilting of the Dirac cone, signaling a nodal line along $K - H$ and allowing the Hamiltonian to be further simplified as:

$$H_K(\mathbf{q}) = q_x\sigma_x + q_y\sigma_y. \quad (14)$$

The eigenstate of the upper/lower branch is

$$\psi^{\text{up/dn}} = \frac{1}{\sqrt{2}} \begin{pmatrix} e^{\pm i\phi_{\mathbf{q}}} \\ 1 \end{pmatrix}, \quad (15)$$

where $\phi_{\mathbf{q}} = \arctan d_y(\mathbf{q})/d_x(\mathbf{q})$ and $\mathbf{d}(\mathbf{q}) = (\cos \phi_{\mathbf{q}} \quad \sin \phi_{\mathbf{q}} \quad 0)$.

For magnons, the DSF adopts the same formal expression as that of phonons in Eq. (7), with the distinction lying in the specific form of $\mathbf{V}(\mathbf{G}) = 2(\cos(g_z\pi) \quad 0 \quad 0)$ (Details are in the supplementary). Specifically, for Gd, we have

$$S_{\text{coh}}^{\text{up/dn}}(\mathbf{Q}, \omega) \propto |F_{\text{coh}}^{\text{up/dn}}(\mathbf{Q})|^2 = 1 \pm (-1)^{g_z} \cos \phi_{\mathbf{q}}. \quad (16)$$

Thus, the DSF of the node-line magnon, shown in Fig. 4(c), exhibits a $\cos \phi_{\mathbf{q}}$ -like dependence on the constant-energy surface in momentum space, while the factor $(-1)^{g_z}$ leads to alternating intensity between the upper and lower bands as the

momentum crosses the Brillouin zone boundary along g_z direction, matching with the observation in experiments [58].

In the pseudospin representation, the QMT takes a particularly simple form, $g_{\pm}^{ab} = \frac{1}{4}(\partial_a \phi_{\mathbf{q}})(\partial_b \phi_{\mathbf{q}})$, from which the full tensor structure follows straightforwardly:

$$g_{\pm} = \frac{1}{4|\mathbf{q}|^4} \begin{pmatrix} q_y^2 & -q_x q_y \\ -q_x q_y & q_x^2 \end{pmatrix}. \quad (17)$$

Figures 4(e)–(f) display g^{yy} on a constant-energy surface in momentum space and along $\Gamma - K$, respectively. Along $\Gamma - K$, $g_{\pm}^{yy} = \frac{q_x^2}{4|\mathbf{q}|^4} \propto \frac{1}{q_x^2}$ leading to a pronounced enhancement near the K point and a vanishing value along the q_z axis.

Since the topological invariant of the node-line magnon is given by the Berry phase, we express this invariant in terms of the pseudospin texture.

$$\gamma_{\pm} = \mp \frac{1}{2} \oint_C \nabla_{\mathbf{q}} \phi_{\mathbf{q}} \cdot d\mathbf{q} = \mp \pi. \quad (18)$$

This formulation reflects a generic property of nodal lines and can be directly accessed experimentally through the DSF.

VII. CONCLUSION

In summary, we establish the dynamical structure factor as a direct experimental probe of both the Berry curvature and quantum metric, enabling complete access to the quantum geometric tensor across the Brillouin zone. Validated in twofold quadruple Weyl phonons and node-line magnons, our approach unifies experimentally measurable scattering intensities with quantum geometry through a pseudospin framework and is readily extendable to multi-band systems with well-defined pseudospin degrees of freedom. By directly linking the DSF to quantum geometry, our work enables experimental access not only to spectral properties but also to geometric and topological responses, including sensitivity to perturbations, topology-induced mode dynamics, enhanced transport, and Chern numbers, thereby establishing a general paradigm for exploring quantum-geometric phenomena in bosonic quasiparticles and paving the way for understanding its role in condensed matter systems.

VIII. NOTE ADDED

We note a related work on the resolution of topology and geometry from momentum-resolved spectroscopies [68].

IX. ACKNOWLEDGEMENTS

We acknowledge the helpful discussion with H. Miao. T. Zhang and C. Wu acknowledge the support from National Key R&D Project (Grant Nos. 2023YFA1407400 and 2024YFA1409200), and the National Natural Science Foundation of China (Grant Nos. 12374165 and 12447101).

T.O. acknowledge support from JSPS KAKENHI (No. JP23H04865, No. 23K22487), MEXT, Japan. S.M. is supported by JSPS KAKENHI Grant Nos. JP22H00108 and JP24H02231, and also by MEXT Initiative to Establish Next-generation Novel Integrated Circuits Centers (X-NICS) Grant No. JPJ011438.

[1] M. V. Berry, Quantal phase factors accompanying adiabatic changes, *Proceedings of the Royal Society of London. A. Mathematical and Physical Sciences* **392**, 45 (1984).

[2] M. V. Berry, The quantum phase, five years after, *Geometric phases in physics* **5**, 7 (1989).

[3] J. Yu, B. A. Bernevig, R. Queiroz, E. Rossi, P. Törmä, and B.-J. Yang, Quantum geometry in quantum materials, *npj Quantum Materials* **10**, 101 (2025).

[4] J. Provost and G. Vallee, Riemannian structure on manifolds of quantum states, *Communications in Mathematical Physics* **76**, 289 (1980).

[5] R. Cheng, Quantum geometric tensor (Fubini-Study Metric) in simple quantum system: A pedagogical introduction, *arXiv preprint arXiv:1012.1337* (2010).

[6] Quantized Hall conductance in a two-dimensional periodic potential, *Physical review letters* **49**, 405 (1982).

[7] D. Xiao, M.-C. Chang, and Q. Niu, Berry phase effects on electronic properties, *Reviews of modern physics* **82**, 1959 (2010).

[8] M.-C. Chang and Q. Niu, Berry curvature, orbital moment, and effective quantum theory of electrons in electromagnetic fields, *Journal of Physics: Condensed Matter* **20**, 193202 (2008).

[9] I. Sodemann and L. Fu, Quantum nonlinear Hall effect induced by Berry curvature dipole in time-reversal invariant materials, *Physical review letters* **115**, 216806 (2015).

[10] A. Gao, Y.-F. Liu, J.-X. Qiu, B. Ghosh, T. V. Trevisan, Y. Onishi, C. Hu, T. Qian, H.-J. Tien, S.-W. Chen, *et al.*, Quantum metric nonlinear hall effect in a topological antiferromagnetic heterostructure, *Science* **381**, 181 (2023).

[11] N. Wang, D. Kaplan, Z. Zhang, T. Holder, N. Cao, A. Wang, X. Zhou, F. Zhou, Z. Jiang, C. Zhang, *et al.*, Quantum-metric-induced nonlinear transport in a topological antiferromagnet, *Nature* **621**, 487 (2023).

[12] X.-B. Qiang, T. Liu, Z.-X. Gao, H.-Z. Lu, and X. Xie, A clarification on quantum-metric-induced nonlinear transport, *Advanced Science* , e14818.

[13] Y. Gao, S. A. Yang, and Q. Niu, Field induced positional shift of bloch electrons and its dynamical implications, *Physical review letters* **112**, 166601 (2014).

[14] J. Han, T. Uchimura, Y. Araki, J.-Y. Yoon, Y. Takeuchi, Y. Yamane, S. Kanai, J. Ieda, H. Ohno, and S. Fukami, Room-temperature flexible manipulation of the quantum-metric structure in a topological chiral antiferromagnet, *Nature Physics* **20**, 1110 (2024).

[15] H. Liu, J. Zhao, Y.-X. Huang, W. Wu, X.-L. Sheng, C. Xiao, and S. A. Yang, Intrinsic second-order anomalous Hall effect and its application in compensated antiferromagnets, *Physical Review Letters* **127**, 277202 (2021).

[16] F. Xie, Z. Song, B. Lian, and B. A. Bernevig, Topology-bounded superfluid weight in twisted bilayer graphene, *Physical Review Letters* **124**, 167002 (2020).

[17] H. Tian, X. Gao, Y. Zhang, S. Che, T. Xu, P. Cheung, K. Watanabe, T. Taniguchi, M. Randeria, F. Zhang, *et al.*, Evidence for dirac flat band superconductivity enabled by quantum geometry, *Nature* **614**, 440 (2023).

[18] L. Liang, T. I. Vanhala, S. Peotta, T. Siro, A. Harju, and P. Törmä, Band geometry, berry curvature, and superfluid weight, *Physical Review B* **95**, 024515 (2017).

[19] J. Yu, C. J. Ciccarino, R. Bianco, I. Errea, P. Narang, and B. A. Bernevig, Non-trivial quantum geometry and the strength of electron-phonon coupling, *Nature Physics* **20**, 1262 (2024).

[20] S. Peotta and P. Törmä, Superfluidity in topologically nontrivial flat bands, *Nature communications* **6**, 8944 (2015).

[21] A. Julku, S. Peotta, T. Vanhala, D.-H. Kim, and P. Törmä, Geometric origin of superfluidity in the Lieb lattice flat band, *arXiv preprint arXiv:1603.03237* (2016).

[22] J. Herzog-Arbeitman, V. Peri, F. Schindler, S. D. Huber, and B. A. Bernevig, Superfluid weight bounds from symmetry and quantum geometry in flat bands, *Physical review letters* **128**, 087002 (2022).

[23] J. S. Hofmann, E. Berg, and D. Chowdhury, Superconductivity, charge density wave, and supersolidity in flat bands with a tunable quantum metric, *Physical review letters* **130**, 226001 (2023).

[24] S. Peotta, K.-E. Huhtinen, and P. Törmä, Quantum geometry in superfluidity and superconductivity, *arXiv preprint arXiv:2308.08248* (2023).

[25] Z.-T. Sun, R.-P. Yu, S. A. Chen, J.-X. Hu, and K. Law, Flat-band floo state from quantum geometric discrepancy, *arXiv preprint arXiv:2408.00548* (2024).

[26] T. Kitamura, A. Daido, and Y. Yanase, *Quantum geometry in correlated electron phases: from flat band to dispersive band* (2025), [arXiv:2512.21206 \[cond-mat.str-el\]](https://arxiv.org/abs/2512.21206).

[27] J.-W. Rhim, K. Kim, and B.-J. Yang, Quantum distance and anomalous landau levels of flat bands, *Nature* **584**, 59 (2020).

[28] Y. Hwang, J.-W. Rhim, and B.-J. Yang, Geometric characterization of anomalous landau levels of isolated flat bands, *Nature communications* **12**, 6433 (2021).

[29] J. Jung, H. Lim, and B.-J. Yang, Quantum geometry and landau levels of quadratic band crossings, *Physical Review B* **109**, 035134 (2024).

[30] A. Srivastava and A. Imamoğlu, Signatures of bloch-band geometry on excitons: nonhydrogenic spectra in transition-metal dichalcogenides, *Physical review letters* **115**, 166802 (2015).

[31] C. Paiva, T. Holder, and R. Ilan, Shift and polarization of excitons from quantum geometry, *arXiv preprint arXiv:2408.10300* (2024).

[32] X. Ying and K. T. Law, Flat band excitons and quantum metric, *arXiv preprint arXiv:2407.00325* (2024).

[33] N. Verma, D. Guerci, and R. Queiroz, Geometric stiffness in interlayer exciton condensates, *Physical Review Letters* **132**, 236001 (2024).

[34] T. Neupert, C. Chamon, and C. Mudry, Measuring the quantum geometry of bloch bands with current noise, *Physical Review B—Condensed Matter and Materials Physics* **87**, 245103 (2013).

[35] F. Piéchon, A. Raoux, J.-N. Fuchs, and G. Montambaux, Geometric orbital susceptibility: Quantum metric without Berry curvature, *Physical Review B* **94**, 134423 (2016).

[36] Y. Gao, S. A. Yang, and Q. Niu, Geometrical effects in orbital magnetic susceptibility, *Physical Review B* **91**, 214405 (2015).

[37] V. V. Albert, B. Bradlyn, M. Fraas, and L. Jiang, Geometry and response of lindbladians, *Physical Review X* **6**, 041031 (2016).

[38] M. Kolodrubetz, D. Sels, P. Mehta, and A. Polkovnikov, Geometry and non-adiabatic response in quantum and classical systems, *Physics Reports* **697**, 1 (2017).

[39] T. Ozawa, Steady-state Hall response and quantum geometry of driven-dissipative lattices, *Physical Review B* **97**, 041108 (2018).

[40] O. Bleu, G. Malpuech, Y. Gao, and D. Solnyshkov, Effective theory of nonadiabatic quantum evolution based on the quantum geometric tensor, *Physical Review Letters* **121**, 020401

(2018).

[41] Y. Li, Y. Liu, and C.-C. Liu, [Unconventional magneto-optical effects in altermagnets](#) (2025), arXiv:2512.03435 [cond-mat.mtrl-sci].

[42] Z. Ouyang, W.-J. Dai, Z.-T. Sun, J.-X. Hu, and K. T. Law, [Quantum geometric planar magnetotransport: a probe for magnetic geometry in altermagnets](#) (2025), arXiv:2512.03814 [cond-mat.mes-hall].

[43] N. Paul, Area-law entanglement from quantum geometry, *Physical Review B* **109**, 085146 (2024).

[44] P. M. Tam, J. Herzog-Arbeitman, and J. Yu, Corner charge fluctuation as an observable for quantum geometry and entanglement in two-dimensional insulators, *Physical Review Letters* **133**, 246603 (2024).

[45] L. Zhou, Quantum geometry and geometric entanglement entropy of one-dimensional floquet topological matter, *Physical Review B* **110**, 054310 (2024).

[46] T. Bzdušek, From quantum geometry to non-linear optics and gerbes: Recent advances in topological band theory, arXiv preprint arXiv:2511.20608 (2025).

[47] G. Pellitteri, Z. Dai, H. Hu, Y. Jiang, G. Menichetti, A. Tomadin, B. A. Bernevig, and M. Polini, Phonon spectra, quantum geometry, and the Goldstone theorem, *Physical Review B* **112**, 10.1103/jg8x-l6h6 (2025).

[48] Y. Li and C.-C. Liu, Quantum metric-based optical selection rules, arXiv preprint arXiv:2507.09260 (2025).

[49] X. Tan, D.-W. Zhang, Z. Yang, J. Chu, Y.-Q. Zhu, D. Li, X. Yang, S. Song, Z. Han, Z. Li, *et al.*, Experimental measurement of the quantum metric tensor and related topological phase transition with a superconducting qubit, *Physical Review Letters* **122**, 210401 (2019).

[50] M. Yu, P. Yang, M. Gong, Q. Cao, Q. Lu, H. Liu, S. Zhang, M. B. Plenio, F. Jelezko, T. Ozawa, *et al.*, Experimental measurement of the quantum geometric tensor using coupled qubits in diamond, *National Science Review* **7**, 254 (2020).

[51] A. Gianfrate, O. Bleu, L. Dominici, V. Ardizzone, M. De Giorgi, D. Ballarini, G. Lerario, K. West, L. Pfeiffer, D. Solnyshkov, *et al.*, Measurement of the quantum geometric tensor and of the anomalous Hall drift, *Nature* **578**, 381 (2020).

[52] G. Sala, M. T. Mercaldo, K. Domi, S. Gariglio, M. Cuoco, C. Ortix, and A. D. Caviglia, The quantum metric of electrons with spin-momentum locking, *Science* **389**, 822 (2025).

[53] M. Kang, S. Kim, Y. Qian, P. M. Neves, L. Ye, J. Jung, D. Puntel, F. Mazzola, S. Fang, C. Jozwiak, *et al.*, Measurements of the quantum geometric tensor in solids, *Nature Physics* **21**, 110 (2025).

[54] S. Kim, Y. Chung, Y. Qian, S. Park, C. Jozwiak, E. Rotenberg, A. Bostwick, K. S. Kim, and B.-J. Yang, Direct measurement of the quantum metric tensor in solids, *Science* **388**, 1050 (2025).

[55] K. Sturm, Dynamic structure factor: An introduction, *Zeitschrift für Naturforschung A* **48**, 233 (1993).

[56] T. Zhang, R. Takahashi, C. Fang, and S. Murakami, Twofold quadruple Weyl nodes in chiral cubic crystals, *Physical Review B* **102**, 125148 (2020).

[57] H. Li, T. Zhang, A. Said, Y. Fu, G. Fabbri, D. G. Mazzone, J. Zhang, J. Lapano, H. N. Lee, H. Lei, *et al.*, Observation of a chiral wave function in the twofold-degenerate quadruple Weyl system BaPtGe, *Physical Review B* **103**, 184301 (2021).

[58] A. Scheie, P. Laurell, P. A. McClarty, G. E. Granroth, M. B. Stone, R. Moessner, and S. E. Nagler, Dirac magnons, nodal lines, and nodal plane in elemental gadolinium, *Physical Review Letters* **128**, 097201 (2022).

[59] A. Kotani and S. Shin, Resonant inelastic x-ray scattering spectra for electrons in solids, *Reviews of Modern Physics* **73**, 203 (2001).

[60] L. J. Ament, M. Van Veenendaal, T. P. Devereaux, J. P. Hill, and J. Van Den Brink, Resonant inelastic x-ray scattering studies of elementary excitations, *Reviews of Modern Physics* **83**, 705 (2011).

[61] G. Benedek and J. P. Toennies, Helium atom scattering spectroscopy of surface phonons: genesis and achievements, *Surface science* **299**, 587 (1994).

[62] B. S. Hudson, Vibrational spectroscopy using inelastic neutron scattering: Overview and outlook, *Vibrational spectroscopy* **42**, 25 (2006).

[63] Z. Jin, B. Hu, Y. Liu, Y. Li, T. Zhang, K. Iida, K. Kamazawa, A. I. Kolesnikov, M. B. Stone, X. Zhang, *et al.*, Chern numbers of topological phonon band crossing determined with inelastic neutron scattering, *Physical Review B* **106**, 224304 (2022).

[64] T. Ozawa and B. Mera, Relations between topology and the quantum metric for chern insulators, *Physical Review B* **104**, 045103 (2021).

[65] T. Liu, X.-B. Qiang, H.-Z. Lu, and X. Xie, Quantum geometry in condensed matter, *National Science Review* **12**, nwae334 (2025).

[66] R. Roy, Band geometry of fractional topological insulators, *Physical Review B* **90**, 165139 (2014).

[67] A. Scheie, P. Laurell, P. A. McClarty, G. E. Granroth, M. B. Stone, R. Moessner, and S. E. Nagler, Spin-exchange hamiltonian and topological degeneracies in elemental gadolinium, *Physical Review B* **105**, 104402 (2022).

[68] S. Huang and C. Fang, [Resolution of topology and geometry from momentum-resolved spectroscopies](#) (2026), arXiv:2601.10677 [cond-mat.mes-hall].

[69] X. Wang, J. R. Yates, I. Souza, and D. Vanderbilt, Ab initio calculation of the anomalous hall conductivity by wannier interpolation, *Physical Review B—Condensed Matter and Materials Physics* **74**, 195118 (2006).

[70] G. L. Squires, *Introduction to the theory of thermal neutron scattering* (Courier Corporation, 1996).

[71] S. Shivam, R. Coldea, R. Moessner, and P. McClarty, Neutron scattering signatures of magnon weyl points, arXiv preprint arXiv:1712.08535 (2017).

[72] M. Bjerngaard, B. Galilo, and A. M. Turner, Neutron scattering off weyl semimetals, *Physical Review B* **102**, 035122 (2020).

[73] T. Zhang, Y. Liu, H. Miao, and S. Murakami, [Advances in phonons: From band topology to phonon chirality](#) (2025), arXiv:2505.06179 [cond-mat.mtrl-sci].

[74] B. Yuan, Y. Bai, Y. Dai, B. Huang, and C. Niu, Prediction of a topological magnon insulator in a two-dimensional chern ferromagnet v2ws4 monolayer, *Nano Letters* **25**, 14436 (2025).

[75] Z. Zhang, Z.-M. Yu, G.-B. Liu, and Y. Yao, Magnetictb: A package for tight-binding model of magnetic and non-magnetic materials, *Computer Physics Communications* **270**, 108153 (2022).

[76] T. Yusufaly, D. Vanderbilt, and S. Coh, Tight-binding formalism in the context of the pythtb package, URL <https://www.physics.rutgers.edu/pythtb/formalism.html> (2013).